MASTERARBEIT | MASTER'S THESIS

Titel | Title

Nanodispersions in Ternary Systems of Thymol, Ethanol and Water

verfasst von | submitted by

Elias Plöchl BEd

angestrebter akademischer Grad | in partial fulfilment of the requirements for the degree of

Master of Education (MEd)

Wien | Vienna, 2025

Studienkennzahl lt. Studienblatt | Degree programme code as it appears on the student record sheet:	UA 199 510 523 02
Studienrichtung lt. Studienblatt | Degree programme as it appears on the student record sheet:	Masterstudium Lehramt Sek (AB) Unterrichtsfach Geographie und wirtschaftliche Bildung Unterrichtsfach Physik
Betreut von | Supervisor:	ao. Univ.-Prof. Mag. Dr. Bogdan Sepiol

Abstract

This thesis investigates the dispersion behavior and particle properties of ternary systems composed of thymol, ethanol, and water, with a focus on their relevance for pharmaceutical applications. Dynamic light scattering (DLS) was used to analyze particle formation under various compositions. Both spontaneous and non-spontaneous particle formation were examined, alongside temperature-dependent measurements. DLS results indicated that, depending on composition, the system formed particles in both the nanometer and micrometer range, also making them accessible to optical microscopy. Subsequent imaging revealed that these compositions show emulsion-like behavior, forming liquid droplets. The ease with which these dispersions can be formed into nanometer-sized liquid droplets suggests their potential for use in the pharmaceutical industry.

Zusammenfassung

Diese Arbeit untersucht das Dispersionsverhalten und die Eigenschaften von Partikeln in ternärer Systemem aus Thymol, Ethanol und Wasser, mit besonderem Fokus auf deren Relevanz für pharmazeutische Anwendungen. Die Bildung von Partikeln wurde bei verschiedenen Zusammensetzungen mithilfe dynamischer Lichtstreuung (DLS) untersucht. Sowohl spontane als auch nicht-spontane Partikelbildung sowie temperaturabhängige Effekte wurden untersucht. Die DLS-Ergebnisse zeigten, dass das System in Abhängigkeit von der Zusammensetzung Partikel im Nano- bis Mikrometerbereich bildet, wodurch eine Untersuchung mittels optischer Mikroskopie möglich wurde. Dabei zeigten sich bei bestimmten Zusammensetzungen flüssige Tröpfchen, die auf ein emulsionsähnliches Verhalten hinweisen. Die einfache Herstellung sowie die Bildung nanometergroßer Flüssigkeitströpfchen deuten auf Potenzial dieser Systeme für pharmazeutische Anwendungen hin.

Danksagung

Ich möchte mich herzlich bei meinem Betreuer, Bogdan Sepiol, bedanken. Seine Freundlichkeit, seine stetige Unterstützung und die Möglichkeit, in seiner Arbeitsgruppe mitarbeiten zu dürfen, haben mir sehr viel bedeutet. Seine wertvolle Anleitung und Ermutigung waren für das Gelingen dieser Arbeit von großer Bedeutung.

Mein besonderer Dank gilt auch Martin, der mich in allen Phasen dieser Arbeit begleitet hat. Ich schätze seine Geduld, die vielen anregenden Gespräche und seinen Einsatz, gemeinsam mit mir neue Ideen auszuprobieren und Lösungen zu finden. Und natürlich auch seine Bemühungen in der Weiterentwicklung meiner musikalischen Horizonte.

Ebenso gilt mein tief empfundener Dank meiner Mutter für ihre Unterstützung während meines gesamten Studiums sowie meiner Partnerin Sabrin, die mir stets zur Seite stand und mich auf diesem Weg immer wieder ermutigt und motiviert hat.

List of Figures

List of Abbreviations

DLS Dynamic Light Scattering

KWW Kohlrausch William Watts

MIC Minimum Inhibitory Concentration

ACF Autocorrelation Function

LSW Lifshitz–Slesov–Wagner

Contents

1. Introduction

Thymol is the primary phenolic compound found in essential oils extracted from thyme. In recent years, interest in thymol has grown significantly within the medical field due to its demonstrated anti-inflammatory, antifungal, and antibacterial properties. The antibacterial properties of thymol are of particular interest, as emerging research suggests it may serve as a potential bioactive compound in pharmaceutical applications. This is especially relevant given the growing threat of multidrug-resistant microorganisms. [1] To increase antibacterial efficacy and reduce potential toxicity and other side effects nanoparticles have been shown to be a suitable carrier for drug delivery [2]. These particles are produced through nano emulsification, a process that creates emulsions with droplet sizes typically ranging from 20 to 500 nm. [3]. Previous studies have examined thymol–ethanol–water systems incorporating surfactants, to enhance particle stability, but research suggests that the inclusion of surfactants may diminish thymol's antimicrobial efficacy [4]. This highlights the importance of exploring emulsion formation without surfactants, both to preserve thymol's therapeutic efficacy and to simplify preparation. The research will therefore focus on the properties of emulsions in a ternary system consisting of thymol, ethanol and water, investigating how factors such as solvent concentration and temperature influence particle size and stability. These effects will be analyzed using dynamic light scattering (DLS), a method that measures the intensity of light scattered by particles within the emulsion. The key quantity of interest is the time it takes for the scattered light intensity to become uncorrelated with its initial value. This decay is driven by particle motion, which, in the case of nanoparticles suspended in a liquid, is governed by diffusion. With all this in mind, the following theory section is structured accordingly: it begins with a discussion of particle formation in ternary systems, followed by an introduction to DLS. Since diffusion is the fundamental mechanism behind particle motion, its role is explored first, along with its influence on particle position over time. The section concludes by establishing a link between these spatial correlations and the scattering of light.

2. Theory

2.1. Particle Formation in Ternary Systems

In ternary systems emulsification can occur where one component (A) acts as a cosolvent that is miscible with two other components (B and C), even though B and C are otherwise immiscible. When B is added to a pre-mixed solution of A and C, it preferentially mixes with A, reducing A's ability to solubilize C. As a result, component C becomes supersaturated and separates into a distinct phase, forming droplets — a process known as spontaneous emulsification or *ouzo effect* [5]. In the case of an thymol-ethanol-water system, ethanol would correspond to liquid A, water to liquid B and thymol to substance C.

Whether this process occurs spontaneously or requires an external energy input depends on the energy cost associated with increasing the interfacial area ΔA between the immiscible substances, as well as the entropy of dispersion, represented by the term $T\Delta S$. This relationship can be described using the change in Gibbs free energy ΔG [6]:

$$\Delta G = \gamma \Delta A - T\Delta S \tag{1}$$

Here, T denotes the absolute Temperature and γ the interfacial tension. Figure 1 depicts these types of formation processes in more detail.

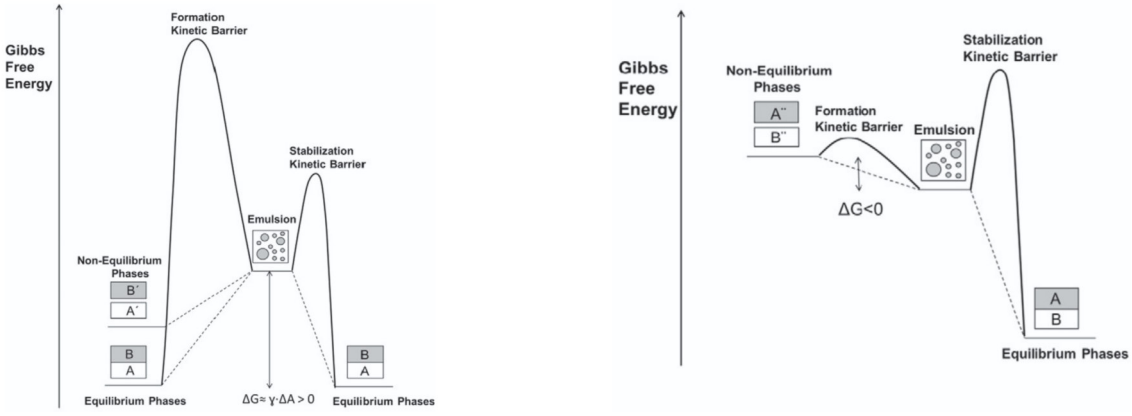

(a) Emulsion requiring external energy input.

(b) Spontaneous emulsion formation.

Figure 1: Schematics of Gibbs free energy and emulsion formation.
Reprinted from [6], with permission from Elsevier.

Figure 1a depicts the non-spontaneous formation process. The total Gibbs free energy is positive in this case, meaning that the change in surface area cannot be energetically overcome by the entropy change. This means external energy input, such as stirring or sonication is required. If the phases are not in equilibrium (1b), then negative values of G may occur, which leads to spontaneous emulsification.

Of course it is also the composition of the different phases, that determine wether emulsification can occur. This is typically depicted in an ternary phase diagram, depicting the different weight percentages of the composites. Figure 2 shows a diagram of an oil-ethanol-water system.

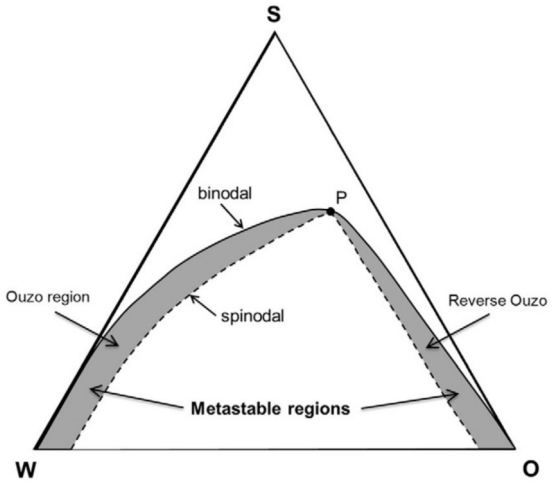

Figure 2: Phase diagram for an oil, ethanol, water system. Reprinted from [6], with permission from Elsevier.

The solid line represents the binodal line, above it, all components are miscible, while below the mixtures separate into a metastable configuration. The dashed line is the spinodal line, which divides the meta stable region from the fully unstable composition, where phase separation always occurs. Emulsification is generally only possible at compositions that lie in the area between these lines. [6]

While these emulsions in general can be kinetically stable, there are two well-known irreversible processes that lead to growth processes inside the emulsion. Coalescence and Oswald ripening. Coalescence occurs when colliding droplets merge into a single drop after the thin film of continuous phase between them ruptures, while Oswald ripening results from the different solubility of small and large particles. [7] Oswald ripening can be assessed quantitatively using the Lifshitz–Slesov–Wagner (LSW) Theorem, which states, that the cube of the particle radius is proportional to time [8]:

$$r^3 = \frac{8}{9}\left(\frac{c(\infty)\gamma V_m D}{\rho R T}\right) t \tag{2}$$

Where c is the solubility and V_m the molar volume of the dispersed phase. For coalescence the particle radii change linearly with time, assuming volume conservation and efficient merging upon collision. [7]

Coarsening phenomena similar to those in emulsion can also occur in alloys. X-ray photon correlation fluctuation analysis, for example, has been used to distinguish between LSW and coagulation mechanisms in alloys, as demonstrated for Al-Ag and Al-Zn systems. [9]

2.2. Dispersion Behavior of Thymol, Water and Ethanol Systems

The phase diagram and therefore the dispersion behavior of thymol, ethanol and water systems has not yet been experimentally investigated in previous studies. A typical emulsion usually involves a liquid-liquid dispersion but the phase behavior of the thymol–ethanol composite upon dilution into water is unclear due to thymol's nature as a crystalline with oil-like solubility characteristics [10]. Unlike classical ternary systems used for emulsions, in which the dispersed phase is a liquid oil at room temperature, thymol is solid under ambient conditions, but fully soluble in ethanol, making it unclear whether droplet formation arises from liquid–liquid phase separation or nanoprecipation. During mixing with water, residual ethanol may locally solvate thymol, allowing for the formation of liquid-like droplets rather than immediate crystallization or solid precipitation. This behavior would align with prior observations for low molecular weight hydrophobic compounds such as β-carotene and cholesteryl acetate, where high supersaturation and rapid solvent exchange result in the formation of amorphous or liquid-like particles instead of crystalline solids. [2]. The type of dispersion formed under these conditions can be examined using a standard light microscope, provided the particle size, determined by DLS, falls within the optical resolution range

The following sections draw heavily from the works of [11], [12],[13], [14] and [15], which provide treatment of the underlying theory.

2.3. Diffusion

The dynamics of emulsions are primarily determined by diffusion processes. Consequently, all subsequent theoretical developments, as well as the dynamic light scattering used to analyze these dynamics, are fundamentally rooted in diffusion theory. A central concept in this theory is the diffusion differential equation, which describes how particle concentration varies in time and space. It is given as:

$$\frac{\partial c(\boldsymbol{r},t)}{\partial t} = D\Delta c(\boldsymbol{r},t) \tag{3}$$

Where $c(x,\boldsymbol{r})$ denotes the function, which describes the concentration of some diffusing substance and D denotes the diffusion coefficient. If the initial condition $c(\boldsymbol{r},0) = \delta(\boldsymbol{r})$ is assumed, the solution of the general equation is given as:

$$c(\boldsymbol{r},t) = \left(\frac{1}{\sqrt{4\pi Dt}}\right)^{\frac{3}{2}} e^{-\left(\frac{|\boldsymbol{r}|^2}{4Dt}\right)} \tag{4}$$

A central quantity in dynamic light scattering is the mean square displacement $\langle \Delta r^2(t)\rangle$, which describes the average squared distance that particles have traveled due to diffusion within a substance over a given time. It is defined as:

$$\langle \Delta \boldsymbol{r}^2(t)\rangle = \int |\boldsymbol{r}|^2 c(\boldsymbol{r},t)\ \mathrm{d}\boldsymbol{r} = 6Dt \tag{5}$$

Which will be important later on. This brief discussion of diffusion above follows [16].

2.4. Correlation in Real Space

The question now becomes how information about particle dynamics can be obtained by analyzing diffusive behavior. In the context of DLS, the most central parameter to achieve this is time dependent correlation. Diffusion directly influences the correlation of particle positions in time. By analyzing how long these particle positions stay correlated, it becomes possible to determine the properties of the particles within the emulsion. To introduce correlation, one can begin more generally with a quantity $a_i(t)$, representing a physical property such as mass, velocity or energy in time. Following the treatment in [11] one can then define a function $A(r,t)$ which describes the distribution of this physical quantity at position r and time t, by summing over all particles N with that physical quantity $a_i(t)$:

$$A(\boldsymbol{r},t) = \sum_{i}^{N} a_i(t)\delta((\boldsymbol{r} - \boldsymbol{r}_i(t)) \tag{6}$$

Taking the Fourier transform of this distribution $A(r,t)$ then to results in:

$$A_q(\boldsymbol{r},t) = \sum_{i}^{N} a_i(t)e^{iq\cdot\boldsymbol{r}_i(t)} \tag{7}$$

Using $A(\boldsymbol{r},t)$ once again, and considering the special case where one is not interested in a specific particle property a_i, but rather just the spatial distribution of particles, one can set $a_i = 1$. This leads to the definition of the microscopic particle density $\rho(\boldsymbol{r},t)$:

$$\rho(\boldsymbol{r},t) = \sum_{i}^{N} \delta(\boldsymbol{r} - \boldsymbol{r}_i(t)) \tag{8}$$

Using this we can introduce correlation, which describes how particle positions at different times are statistically related. It is a probability and can be thought of as *measurement in similarity of particle positions at different times.* Correlation of particle density is described

by the Van Hove function $G(\boldsymbol{r}, t)$ [11]:

$$G(\boldsymbol{r}, t) = \left\langle \frac{1}{N} \sum_{i}^{N} \sum_{j}^{N} \delta(\boldsymbol{r} - \boldsymbol{r}_j(t) + \boldsymbol{r}_i(0)) \right\rangle = \frac{1}{\rho} \langle \rho(\boldsymbol{r}, t) \rho(\boldsymbol{r}, 0) \rangle \tag{9}$$

This correlation function can be separated into two terms, one that describes the correlation of the density of a particle with the density of the same particle at a later time $G_s(\boldsymbol{r}, t)$:

$$G_s(\boldsymbol{r}, t) = \left\langle \frac{1}{N} \sum_{i}^{N} \delta(\boldsymbol{r} - \boldsymbol{r}_i(t) + \boldsymbol{r}_i(0) \right\rangle \tag{10}$$

And another function $G_d(\boldsymbol{r}, t)$, that describes the cross correlation of the density of different particles. The sum of these results in the original correlation function:

$$G(\boldsymbol{r}, t) = G_s(\boldsymbol{r}, t) + G_d(\boldsymbol{r}, t) \tag{11}$$

One can again take the spatial Fourier transform of this correlation function, which is called intermediate scattering function $F(\boldsymbol{q}, t)$ [11]:

$$F(\boldsymbol{q}, t) = \int G(\boldsymbol{r}, t) e^{i\boldsymbol{q}\cdot\boldsymbol{r}} \, \mathrm{d}\boldsymbol{r} \tag{12}$$

A generalized concept of time-dependent correlation is now introduced; however, its connection to diffusion and its use for extracting information about particle dynamics remains somewhat abstract at this point. To make this connection meaningful, it is necessary to relate the correlation function explicitly to diffusion. In the case of a dilute suspension connecting the correlation function to diffusion is straightforward. In such systems, particle interactions are negligible, and therefore cross-correlations between distinct particles can be ignored. The intermediate scattering function then reduces to the self intermediate

scattering function, which is the Fourier transform of the self part of the Van Hove function $G_s(\boldsymbol{r}, t)$ [11]:

$$F_s(\boldsymbol{q}, t) = \int G_s(\boldsymbol{r}, t)\, e^{i\boldsymbol{q}\cdot\boldsymbol{r}}\, \mathrm{d}\boldsymbol{r} \tag{13}$$

Inserting the definition of $G_s(\boldsymbol{r}, t)$, obtained in equation (10) can then be written as:

$$F_s(\boldsymbol{q}, t) = \left\langle \frac{1}{N} \sum_{i=1}^{N} \int \delta(\boldsymbol{r} - [\boldsymbol{r}_i(t) - \boldsymbol{r}_i(0)])\, e^{i\boldsymbol{q}\cdot\boldsymbol{r}}\, \mathrm{d}\boldsymbol{r} \right\rangle \tag{14}$$

Solving the expression by integrating the delta function results in:

$$F_s(\boldsymbol{q}, t) = \left\langle \frac{1}{N} \sum_{i=1}^{N} e^{i\boldsymbol{q}\cdot[\boldsymbol{r}_i(t) - \boldsymbol{r}_i(0)]} \right\rangle \tag{15}$$

Which, because we're only regarding self correlation, simplifies to [13]:

$$F_s(\boldsymbol{q}, t) = \left\langle e^{i\boldsymbol{q}\cdot[\boldsymbol{r}(t) - \boldsymbol{r}(0)]} \right\rangle \tag{16}$$

In the following, $\boldsymbol{r}(t) - \boldsymbol{r}(0)$ is denoted as $\Delta\boldsymbol{r}(t)$, but as established in equation (5) $\langle \Delta\boldsymbol{r}^2(t) \rangle$ results in $6Dt$. Therefore in the Gaußian approximation, this evaluates to [11], [13]:

$$\left\langle e^{i\boldsymbol{q}\cdot\Delta\boldsymbol{r}} \right\rangle = e^{-\frac{1}{2}\langle \boldsymbol{q}^2\cdot\Delta\boldsymbol{r}^2(t) \rangle} = e^{-\boldsymbol{q}^2 Dt} \tag{17}$$

This result links the intermediate scattering function to particle dynamics, as the diffusion coefficient D is directly related to the hydrodynamic radius r and the fluid viscosity η [15].

To summarize:

$$F_s(\boldsymbol{q}, t) = e^{-\boldsymbol{q}^2 D t} \tag{18}$$

Unfortunately, the positional correlations described by the intermediate scattering function cannot be measured directly. Instead, a method is required to relate an experimentally accessible quantity to these correlations. This is where DLS comes into play. It indirectly determines the intermediate scattering function by analyzing fluctuations in scattered light intensity caused by particle motion. [17]

2.5. From Real Space Correlation to Electric Field Correlation

A framework for the correlation in position of particles is now established, which should now be analyzed. This can be done by thinking about the connection between these particles and light interacting with them. It is generally easy to conceptualize, that light scatters, because of some variation in the dielectric constant, which in a condensed system, like an emulsion, can stem from the presence of particles. So the position of these particles will determine the scattered lights field. The sum of electric field amplitude of this scattered light can then be described by [14], [17]:

$$E(\boldsymbol{q}, t) \propto \sum_{i}^{N} e^{-i\boldsymbol{q}\cdot\boldsymbol{r}_i(t)} \tag{19}$$

But it is immediately clear, that this is the Fourier transform of the definition of particle positions in equation (8), as discussed in [14]:

$$E(\boldsymbol{q}, t) = \int \rho(\boldsymbol{r}, t) \cdot e^{-i\boldsymbol{q}\cdot\boldsymbol{r}(t)} \, \mathrm{d}\boldsymbol{r} \tag{20}$$

One can then define time dependent correlation of the electric field similar to what has

been done to correlation in real space with microscopic density, which results in [13]:

$$\frac{\langle E(\boldsymbol{q},t)E(\boldsymbol{q},0)\rangle}{\langle E(\boldsymbol{q},t)^2\rangle} = \left\langle e^{(-i\boldsymbol{q}\cdot[\boldsymbol{r}(0)-\boldsymbol{r}(t)])}\right\rangle \tag{21}$$

Which makes it clear, that the intermediate scattering function $F(\boldsymbol{q},r)$, which is the Fourier transform of the correlation function $G(\boldsymbol{r},t)$ in real space is related to the correlation function of the electric field amplitude, which is denoted as $g^{(1)}(\boldsymbol{q},t)$ [13]:

$$g^{(1)}(\boldsymbol{q},t) = \frac{\langle E(\boldsymbol{q},t)E^*(\boldsymbol{q},0)\rangle}{\langle |E(\boldsymbol{q},0)|^2\rangle} = \frac{F(\boldsymbol{q},t)}{F(\boldsymbol{q},0)} \tag{22}$$

The solution to the scattering function has been determined to be $e^{-D\boldsymbol{q}^2t}$ in equation (17) for a diffusing system. But now the electric field correlation yields an additional result, as for monodisperse particles the electric field amplitude correlation is described by a simple exponential decay [14]. Putting this all together, the electric field amplitude correlation is identical to the intermediate scattering function which both result in some exponential function depending on time:

$$g^{(1)}(\boldsymbol{q},t) = e^{-D\boldsymbol{q}^2t} = e^{\frac{-|t|}{\tau}} \tag{23}$$

Where τ is the correlation time, describing how long it takes for particles to become completely uncorrelated. This results in the following equation that allows for making conclusion on the particle dynamics inside the emulsion:

$$\frac{1}{\tau} = \boldsymbol{q}^2 D \tag{24}$$

D denotes the diffusion coefficient which depends on the particle radius and the viscosity and $\boldsymbol{q}$ is the scattering vector, which depends on the scattering angle ϑ [12]. The diffusion

coefficient for spherical particles in a suspension follows the Einstein-Stokes relation [15]:

$$D = \frac{k_B T}{6\pi\eta R} \tag{25}$$

$$q = \frac{4\pi}{\lambda} \sin\frac{\vartheta}{2} \tag{26}$$

This means, that by determining the correlation time one can determine the particle radius if the viscosity is known and vice versa for a given scattering angle and wavelength. Keeping in mind, that the dependency of wavelength on the refractive index n has to be accounted for:

$$\lambda = \frac{\lambda_0}{n} \tag{27}$$

Equation (24) is derived from the electric field amplitude correlation function, which describes how long the field amplitudes of particles remain correlated. This correlation time is denoted as τ. At the same time, τ is related to the intermediate scattering function, which provides a connection to the diffusion coefficient and the scattering angle. This can be used for an experimental setup: The value of τ can be obtained by calculating the correlation function $g^{(1)}(q,t)$ and fitting an appropriate model to the data. The scattering vector can be determined from the scattering angle and all parameters needed to calculate the diffusion coefficient are known, except for the particle radius and the viscosity. Given either of these quantities, the other can be computed accordingly. [18]

The final challenge lies in the fact that the electric field amplitude correlation function is not directly accessible through experiment. It must be derived indirectly. The key is intensity. It can be determined by analyzing the intensity correlation of the photons scattered by the particles.

2.6. Electric Field Correlation and Intensity Correlation

The following section draws mainly from [13]. The mean intensity of light scattered off of particles can be related to the electric field amplitude of said light through the relation $I(t) = |E(t)|^2 = E(t)E(t)^*$ and equation (19), which under assumption of particle independence results in:

$$\langle I(\boldsymbol{q},t)\rangle = \langle E(\boldsymbol{q},t)E^*(\boldsymbol{q},t)\rangle = \sum_{i=1}^{N}\sum_{j=1}^{N}\langle e^{i\boldsymbol{q}\cdot(\boldsymbol{r}_i(t)-\boldsymbol{r}_j(t))}\rangle = N \tag{28}$$

The goal now is to define a correlation function for the intensity, as was done for the electric field, and to establish a connection between the two. To achieve this one again introduces correlation by comparing a quantity at time t with the same quantity at a later time $t + t'$.This quantity is now Intensity, so it is correlated at $I(\boldsymbol{q}, t)$ to an intensity at a later point time $I(\boldsymbol{q}, t + t')$, which is then given as:

$$\langle I(\boldsymbol{q},t)I(\boldsymbol{q},t+t'\rangle = \lim_{T\to\infty}\frac{1}{T}\int_0^T I(\boldsymbol{q},t)I(\boldsymbol{q},t+t')\,dt \tag{29}$$

Note that, up to this point, all correlation functions have been referenced to the initial time $t = 0$, allowing the correlation time t' to be written simply as t. In what follows, t will be used explicitly referencing the initial time, as this is the usual notation and useful later on. When looking at very large delay times t' where the intensities become uncorrelated, the average can be separated and the equation reduces to:

$$\lim_{t'\to\infty}\langle I(\boldsymbol{q},t)I(\boldsymbol{q},t+t'\rangle = \langle I(\boldsymbol{q},t)\rangle\langle I(\boldsymbol{q},t+t'\rangle = \langle (I(\boldsymbol{q})\rangle^2 \tag{30}$$

In reality one cannot perform an experiment which runs infinitely long. But when measuring several magnitudes longer than the correlation time t', we can use this fact to approximate the correlation function in equation as (29):

$$\langle I(\boldsymbol{q},t)I(\boldsymbol{q},t+t')\rangle = \frac{1}{T-t'}\int_0^{T-t'} I(\boldsymbol{q},t)I(\boldsymbol{q},t+t')dt \tag{31}$$

Now since this is established, we can again relate this intensity correlation function to the electric field using equation (28):

$$\begin{aligned}\langle I(\boldsymbol{q},t)I(\boldsymbol{q},t+t')\rangle &= \left\langle \left(\sum_{j=1}^{N}\sum_{k=1}^{N} e^{-i\boldsymbol{q}\cdot[\boldsymbol{r}_j(0)-\boldsymbol{r}_k(0)]}\right)\left(\sum_{l=1}^{N}\sum_{m=1}^{N} e^{-i\boldsymbol{q}\cdot[\boldsymbol{r}_l(t')-\boldsymbol{r}_m(t')]}\right)\right\rangle \\ &= \sum_{j=1}^{N}\sum_{k=1}^{N}\sum_{l=1}^{N}\sum_{m=1}^{N}\left\langle e^{-i\boldsymbol{q}\cdot[\boldsymbol{r}_j(0)-\boldsymbol{r}_k(0)+\boldsymbol{r}_l(t')-\boldsymbol{r}_m(t')]}\right\rangle\end{aligned} \tag{32}$$

Which, well, is quite an intimidating equation. However, under the assumption that particle positions are completely independent, the expression simplifies drastically. To understand how, one can first look at the average over of the electric field of a particle system:

$$\langle E(\boldsymbol{q},t)\rangle = \sum_{i=1}^{N}\langle e^{i\boldsymbol{q}\cdot\boldsymbol{r}_i(t)}\rangle = \sum_{i=1}^{N}\langle\cos\boldsymbol{q}\ \boldsymbol{r}_i(t)\rangle\langle\sin\boldsymbol{q}\ \boldsymbol{r}_i(t)\rangle = 0 \tag{33}$$

This becomes 0, because as we have established, the position is randomly distributed following a Gaußian distribution. For large particle systems the contributions of each Field cancel out. Now this fact and particle independence will help us simplify equation (32). Looking back at the equation and looking at an unique index $j \neq l,k,m$ (no self correlation), we can factorize the averages, which each become 0 as explained in the previous step. This also makes physical sense, as an independent index translates to uncorrelated particles. If on the other hand we have non-independent indices, one has to look at different cases. By assessing different index combinations one will arrive at the fact that only terms were $j=k$ and $l=m$ or $j=m$ and $k=l$ contribute to the sum [13], resulting in:

$$\langle I(\boldsymbol{q},0)I(\boldsymbol{q},t')\rangle = N + N^2\left|\left\langle e^{(-i\boldsymbol{q}\cdot[\boldsymbol{r}(0)-\boldsymbol{r}(t')])}\right\rangle\right|^2 \tag{34}$$

Now what is left is to normalize this intensity correlation by $\langle I(q,t)\rangle^2$, which is established to be N^2 by equation (28). Which finally allows for the definition of the normalized intensity correlation function $g^{(2)}(t')$:

$$g^{(2)}(t') = \frac{\langle I(\boldsymbol{q},0)I(\boldsymbol{q},t')\rangle}{\langle I(\boldsymbol{q},t)\rangle^2} = 1 + \left|\left\langle e^{(-i\boldsymbol{q}\cdot[\boldsymbol{r}(0)-\boldsymbol{r}(t')])}\right\rangle\right|^2 \tag{35}$$

Which is identical to 1+ the square of the field correlation of the scattered light defined in equation (21):

$$g^{(2)}(\boldsymbol{q},t') = 1 + |g^{(1)}(\boldsymbol{q},t')|^2 \tag{36}$$

Which is often called the *Siegert Relation*. This concludes the theory on DLS. The relation between Intensity and the electric field is now established, which was the final necessary step to connect the diffusion coefficient to a measurable quantity, which finally allows determining the particle radii.

3. Methods

To determine the correlation time τ, the amplitude field correlation function $g^{(1)}(t')$ must first be obtained. However, this function cannot be measured directly. Instead, it can be derived by measuring the intensity and calculating the autocorrelation $g^{(2)}(t')$ of light scattered by particles within the emulsion. The following experimental setup is used for this purpose.

3.1. Experimental Setup and Sample Preparation

Figure 3 depicts the schematic of the experimental setup for all procedures to provide a visual reference for the components and their arrangement.

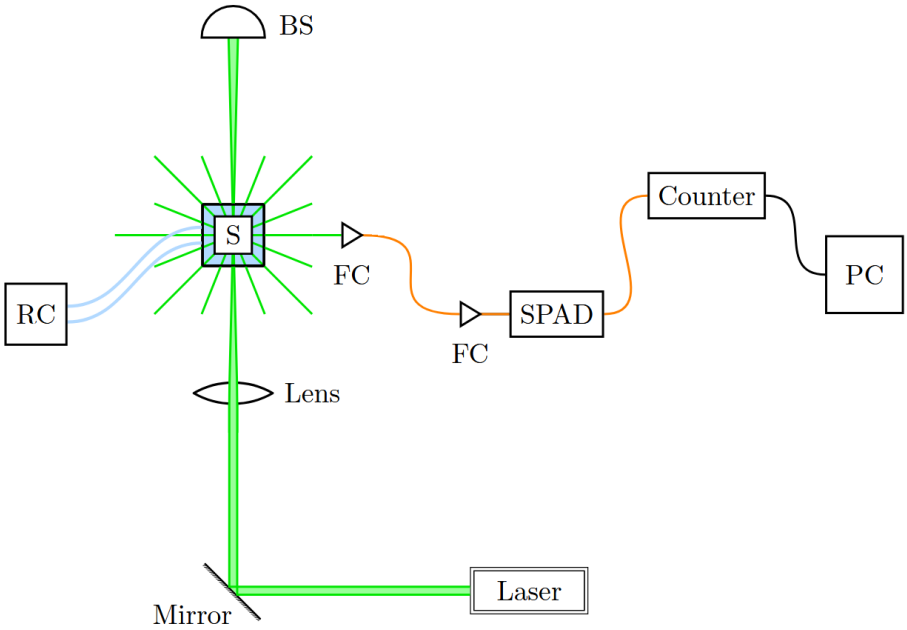

Figure 3: Schematic of the experimental setup used for DLS.

A laser emits light at a wavelength of 528 nm, which is then directed by a mirror into a converging lens. The lens focuses the light onto the sample (S), where it is scattered

in all directions. Any unscattered light that passes through the sample is absorbed by a beam stopper (BS). A portion of the scattered light, at a scattering angle of $\theta = 90°$, is collected by a fiber collimator (FC). It then passes through a single-mode fiber and is emitted by another fiber collimator into a single photon avalanche diode MPD PDM-050-C0C (SPAD), which amplifies the signal to a usable level for detection. The intensity data recorded by the counter, implemented with an NI PCI-6601, which can then be analyzed using a computer (PC). To ensure a stable temperature, the sample is placed in a water bath. The water is pumped through the system by a circulator (RC).

All data derived from this setup is subsequently processed and analyzed using Python. This analysis includes the computation of the autocorrelation functions, fitting appropriate models to the correlation data and visualization (Appendix A).

The photon counter records data as photon counts per time interval in a binary format. This data must then be converted into a readable format, resulting in a array where each element corresponds to the number of photons detected within the time interval, which allows for all subsequent data analysis. It is important to note that the resulting array, depends on the initially chosen channel time or interval, which for most measurements will be set to 30µm.

Sample preparation is a critical step in the experimental procedure, as errors introduced here can lead to systematic deviations in the results. The preparation is carried out as follows. A stock solution of thymol in ethanol is prepared at a fixed ratio of 1:10 (thymol:ethanol by weight). This solution is then transferred into a clean cuvette, followed by the addition of distilled water to reach the desired final concentration. Two important precautions must be taken during this step. First, one must avoid dust contamination, as dust particles are typically several orders of magnitude larger than the target structures and can significantly affect the scattering signal. Second, the procedure should be performed quickly to minimize ethanol evaporation, which could alter the composition and interfere with reproducibility. Once all components are combined, the sample is immediately measured using the described setup. If no spontaneous emulsification is observed, the sample is subjected to sonication using a GT-7810A ultrasonic bath at an electrical power of 50 W and 42 kHz to promote uniform dispersion and, if necessary, provide the energy required to induce emulsification.

If particles in the micrometer range are detected by DLS, microscopic imaging will be conducted using a Zeiss Axio Imager 2.

3.2. Computation of Intensity Correlation

To provide a clearer understanding of the data evaluation presented in the following sections, the key takeaways from the theory section are summarized here. Essentially, the amplitude correlation of the electric field from all nanoparticles in the emulsion is the central data required to draw conclusions about particle size and dynamics. Note, that because the experiment setup is performed at a constant scattering angle $\boldsymbol{q}$, the amplitude correlation, denoted as $g^{(1)}(\boldsymbol{q}, t')$, will simply be written as $g^{(1)}(t')$. It is given as [13]:

$$g^{(1)}(t') = \frac{\langle E(t)E^*(t+t')\rangle}{|\langle E(t)E^*(t)\rangle|}$$

The amplitudes of the electric field are not directly accessible through experiments. However, the intensity of the scattered light, which is proportional to the square of the electric field amplitude, can be measured. The Intensity can be related to the amplitude correlation using the Siegert Relation to arrive at [13]:

$$g^{(2)}(t') = \frac{\langle I(t)I(t+t')\rangle}{\langle I(t)\rangle^2} = 1 + \left|g^{(1)}(t')\right|^2 \tag{37}$$

By measuring the intensity function $I(t)$ over a sufficiently long time period and computing its correlation with the intensity at a later time, $I(t+t')$, we can obtain all the necessary information about the amplitude correlation function. The unnormalized intensity function is given by equation (31) for correlation times several magnitudes smaller than the measurement time. if the intensity function is assumed to be discrete, which in the experiment setup is the case, the intensity correlation can be calculated as follows:

$$\langle I(t)I(t+t')\rangle = \frac{1}{T-t'}\int_0^{T-t'} I(t)I(t+t')\,dt = \frac{1}{N-t'}\sum_{i=1}^{N-t'} I_j(t)I_j(t+t') \tag{38}$$

Where N then denotes the number of time channels. This is the algorithm that can be used to numerically calculate the $g^{(2)}(t')$ function, the correlation is determined by taking

all values of the array up to the $(N - t')$ -th value and multiplying each of these values by the corresponding values in the array starting from $t' + j$. Now the correlation function just needs to be normalized by the squared average. This means that equation (37) can then be written as:

$$\frac{\langle I(t)I(t+t')\rangle}{\langle I(t)\rangle^2} = \frac{1}{N-t'}\sum_{j=1}^{N-t'} I_j I_{j+t'} \times \left[\frac{1}{N}\sum_{j=1}^{N} I_j\right]^{-2}$$

Which is the discrete description of the correlation function. Therefore:

$$g^{(2)}(t') = \frac{1}{N-t'}\sum_{j=1}^{N-t'} I_j I_{j+t'} \times \left[\frac{1}{N}\sum_{j=1}^{N} I_j\right]^{-2}$$

Which is implemented in python to evaluate the acquired intensity data from the experimental setup. As this algorithm shows a time complexity of $O(N^2)$ a faster method is implemented additionally. It is also important to keep in mind that the number of terms used to compute the correlation decreases as t' increases. As a result, the statistical error grows as well with the increase of t'.

To obtain a faster algorithm the fact is used, that the intensity autocorrelation is mathematically equivalent to the convolution of $I(t')$ with it's reversed counterpart $I(-t')$ [19]. therefore the correlation in equation (38) at $t = 0$ can be written as:

$$\langle I(0)I(t')\rangle = \frac{1}{N-t'}\ I(t') * I(-t') = \frac{1}{N-t'}\ (I * I_{rev})(t') \tag{39}$$

While the concept of a negative t' makes no physical sense, as there just is no Intensity at $t < 0$, the connection to convolution allows for faster computation in the Fourier space. By recognizing again that $N >> t'$ where $\frac{1}{N-t'}$ can be approximated as $\frac{1}{N}$ the connection to the frequency domain can be made by the Wiener-Khinchin Theorem [19]:

$$\mathcal{F}\langle I(0)I(t')\rangle = \frac{1}{N}|\mathcal{F}I(t)|^2 \tag{40}$$

The intensity correlation can then be calculated by first taking the Fourier transform of the intensity array, multiplying by the complex conjugate and then taking the inverse transformation:

$$\langle I(0)I(t')\rangle = \frac{1}{N-t'}\ \mathcal{F}^{-1}\{\mathcal{F}I(t)\odot\mathcal{F}^*I(t)\} \tag{41}$$

Where $\mathcal{F}$ and $\mathcal{F}^*$ represent the Fourier transform and the complex conjugate of the Fourier transform respectively. Fourier transformation assumes that the input signal is periodic, meaning that the array will wrap around at the edges when performing convolution in the frequency domain. This can introduce artifacts due to discontinuities at the boundaries of the array. While for $T >> t'$ this step might be redundant it is easily implemented by redefining $I(t)$ as [20]:

$$I_{\text{pad}}(t) = \begin{cases} I(t), & 0 \le t < N \\ 0, & N \le t < 2N \end{cases}$$

Replacing the intensity with its padded form and normalizing the correlation with $\langle I(t)\rangle^2$ results in the final algorithm that is used to calculate intensity autocorrelation:

$$g^{(2)}(t') = \frac{1}{N-t'}\ \mathcal{F}^{-1}\{\mathcal{F}I_{pad}(t)\cdot\mathcal{F}^*I_{pad}(t)\}\times\left[\frac{1}{N}\sum_{i=j}^{N}I_j\right]^{-2} \tag{42}$$

If fast Fourier transform is used for these calculations, one arrives at a time complexity of $O(N\cdot\ln(N))$, which is significantly faster for larger N.

Figure 4 depicts the calculated values of the autocorrelation function for both methods as well as the calculation time for an Intensity with $N = 3 \cdot 10^5$.

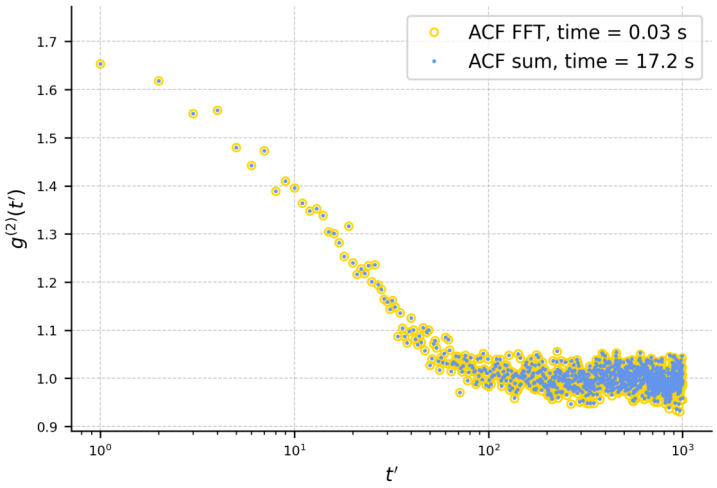

Figure 4: Comparison of autocorrelation functions and computation time. The time t' is measured in channels, where each channels corresponds to 30 µs.

While the algorithm functions as intended and provides the required results, it does generate a significant amount of noise, as evidenced in Figure 4. To address this issue, the algorithm is further extended. To minimize the noise, a binning technique is introduced. Each value of the $g^{(2)}$ function is associated with a specific time interval Δt. For larger values of t', it is possible to reduce the noise by averaging over multiple time intervals. The corresponding $g^{(2)}$ values for these intervals are then averaged together, thereby smoothing the result. This approach is implemented as follows:

First, the bins are defined as B_i, where each bin corresponds to a certain number of t' values. As the time t' increases, the number of t' values in each bin grows at a rate determined by λ. Finally, the bin values are rounded down to the nearest integer to ensure they correspond to a discrete number of t' values:

$$B_i = \sum_{j=1}^{i} \lfloor \Delta t_1 \lambda^{j-1} \rfloor \tag{43}$$

Each bin is then assigned the average of the $g^{(2)}$-values corresponding to the size of the bin, resulting in the binned values $\bar{g}^{(2)}$:

$$\bar{g}_i^{(2)} = \sum_i^N \frac{1}{B_{i+1} - B_i} \sum_{k=B_i}^{B_{i+1}-1} g_k^{(2)} \tag{44}$$

For small growth rates λ, the rounded function can lead to multiple bins with the same value. These multiples are removed. Figure 5 depicts the autocorrelation values using Fourier transform and the binned values for $g^{(2)}$. A growth factor of $\lambda = 1.05$ is used.

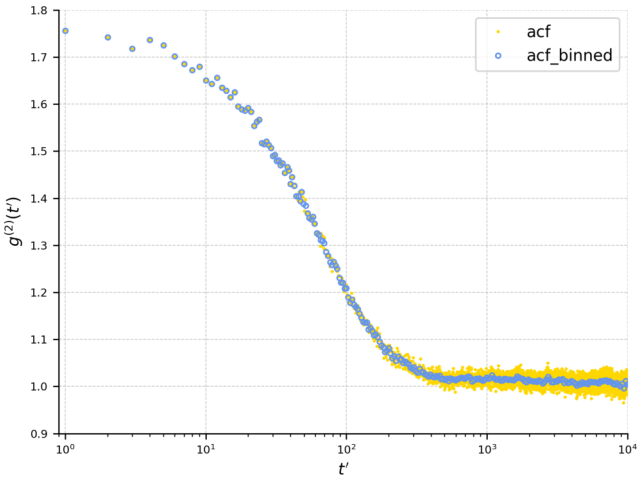

Figure 5: Comparison of binned and unbinned autocorrelation data.

This concludes the section on methods to determine the autocorrelation function. The experimental set up now allows us to determine the intensity function in a given time, which we are now able to process to determine the autocorrelation of this intensity. That means that this correlation data now just needs to be fitted to extract the correlation time to determine the particle radii, which will be discussed in detail later on.

3.3. Computation of total Intensities

While the correlation time is crucial for determining the particle radius, it is also possible to include information from the total measured intensity. In particular, the total intensity is proportional to both the number of particles N and the sixth power of the particle radius

R for particles in the Rayleigh regime:

$$I \propto N \cdot R^6 \tag{45}$$

For larger particles, where the Mie scattering regime is dominant, the scattered light is unequal in energy to the incident light and becomes angle dependent, then the relation in (45) does not hold any longer. [21]

A straightforward way to calculate the total intensity directly from the measured photon array is:

$$I = \sum_{i}^{N} I_i \tag{46}$$

Instead of performing this summation explicitly for each measurement, one can use the fact that the first channel of the Fourier transform, as performed in Equation (42) already provides the same quantity. The discrete Fourier transform is given by [20]:

$$X_k = \sum_{j}^{N-1} I_j \cdot e^{i2\pi kn/N} \tag{47}$$

Where X_k is the Fourier-transformed intensity. Using $k = 0$ yields and identical result to the total intensity in (46). The total intensity is used to get further information on the measured samples.

3.4. Computation of Viscosities

Since the primary goal of this experimental setup is to determine the radius of the particles, it is essential to have accurate knowledge of the viscosity of the emulsion as explained in detail in section 2.5. The emulsion in question is a mixture of ethanol and water, and because viscosity is a non-linear property, the overall viscosity cannot be calculated by simply using a weighted average. Instead, a suitable model must be used to estimate

the viscosity of the mixture η_m. Here, the Jouyban-Acree model is used. It allows for the calculation of the mixture's viscosity based on the known viscosities of the pure components and their concentrations in the solution [22]:

$$\ln \eta_m = X_1 \ln \eta_{1,T} + X_2 \ln \eta_{2,T} + A_0 \left(\frac{X_1 X_2}{T} \right) + A_1 \left(\frac{X_1 X_2 (X_1 - X_2)}{T} \right) + A_2 \left(\frac{X_1 X_2 (X_1 - X_2)^2}{T} \right) \tag{48}$$

Given that the molar masses $X_{1/2}$, viscosities $\eta_{1/2}$, and model constants $A_{0/1/2}$ for ethanol and water are well-documented in the literature such as [23], the calculation of the combined viscosity η_m is then straightforward.

4. Data Analysis

4.1. Modeling the Autocorrelation Data

As outlined in the theory section, the data obtained from the autocorrelation function must be fitted using functions that describe the correlation of electric field amplitudes. For monodisperse particles, Equation (23) is applied, which, when fitting to intensity correlation, results in:

$$g^{(2)}(t') = 1 + |g^{(1)}(t')|^2 = 1 + \beta e^{-\frac{2|t'|}{\tau}} \tag{49}$$

Where β denotes the coherence factor [24]. In general, when fitting autocorrelation data, it is necessary to determine up to which data point the fit should be performed. Typically, a point is chosen where the original amplitude of the correlation has decayed to $\frac{1}{e^2}$. [25] While the assumption of monodispersity and therefore the fit in equation (49) holds for certain emulsions, it is not generally valid, as many emulsions are polydisperse. Therefore, the fitting functions must be adapted accordingly. A simple approach to account for polydispersity is using a Kohlrausch-William-Watts (KWW) function:

$$g^{(2)}(t') = 1 + e^{-2\left(\frac{t'}{\tau}\right)^{\alpha}} \tag{50}$$

where α is a parameter that typically falls within the range $[0, 1]$, where $\alpha = 1$ corresponds to a single exponential decay. If α lies below 1, $g^{(1)}(t')$ follows a stretched exponential decay, meaning it decreases more slowly than a single exponential function. This behavior suggests the presence of a broad distribution of relaxation times [26], [24]. However, while the KWW function often provides a good empirical fit to $|g^1(t')|^2$, interpreting the physical significance of both τ and α can be challenging. Therefore a different approach ist used that takes the distribution of all correlation functions into account. [27]

For a polydisperse emulsion, the amplitude correlation function $g^{(1)}(t')$ is obtained by integrating over all correlation functions, weighted by a distribution $G(\Gamma)$ that describes the individual decay rates corresponding to different particle sizes, which is usually normalized

to arrive at [24]:

$$g^{(1)}(t') = \int_0^\infty G(\Gamma) e^{-\Gamma t'} \mathrm{d}\Gamma \tag{51}$$

Where the distribution $G(\Gamma)$ is normalized:

$$\int_0^\infty G(\Gamma) \mathrm{d}\Gamma = 1 \tag{52}$$

In a polydisperse emulsion, the diffusion coefficient D varies due to the presence of particles of different sizes. Since the decay rate is given by $\Gamma = Dq^2$, it is no longer constant but instead follows a distribution determined by the particle size distribution. The integral describing the amplitude correlation for polydisperse systems reduces to equation (23) when looking at correlation of a monodisperse sample, this is because $G(\Gamma)$ is then described by a delta function centered at Γ_0. This results in:

$$g^{(1)}(t') = \int_0^\infty \delta(\Gamma - \Gamma_0) e^{-\Gamma t'} \mathrm{d}\Gamma = e^{-D_0 \boldsymbol{q}^2 t'} \tag{53}$$

To improve the fitting using this refined amplitude correlation function, one can recognize that it is equivalent to the moment generating function $M(t', \Gamma)$. It is therefore given by [24]:

$$M(-t', \Gamma) = g^{(1)}(t') = \int_0^\infty G(\Gamma) e^{-\Gamma t'} \mathrm{d}\Gamma \tag{54}$$

It is now established that the amplitude correlation is equivalent to the moment generating function, this can be further extended by taking the logarithm of the moment generating function, which is the cumulant function K [28]:

$$K(-t', \Gamma) = \ln\ M(t', \Gamma) = \ln\ g^{(1)}(t') \tag{55}$$

This function characterizes the statistical structure of the decay rate distribution, which modeled as a Gaussian distribution reflects the variation in decay rates due to different particle sizes. This is done by taking the m-th derivative of the cumulant function, which correspond to mean, variance and skewness by order. The m-th derivative is calculated as [29]:

$$K_m(\Gamma) = \frac{\mathrm{d}^m K(-t', \Gamma)}{\mathrm{d}(-t')^m} = (-1)^m\ \frac{\mathrm{d}^m}{\mathrm{d}(t')^m}\ \ln\left[\int_0^\infty G(\Gamma)\ e^{-\Gamma t'}\mathrm{d}\Gamma\right] \tag{56}$$

Using the cumulant generating function $K_m(\Gamma)$, the logarithm of the amplitude correlation function can be expanded as [28]:

$$K(t') = \ln g^{(1)}(t') = \sum_{m=1}^{\infty} \frac{(-t')^m}{m!} K_m = -\bar{\Gamma}t' + \frac{K_2}{2!}t'^2 - \frac{K_3}{3!}t'^3 + \dots \tag{57}$$

Which can be used to directly fit the logarithm of the $g^{(2)}(t')$ function by assuming the baseline B to be exactly one. If the baseline B is not assumed to be exactly one, and nonlinear fitting methods are used, it is more practical to work with the full exponential form of the cumulant expansion. In this case, the intensity autocorrelation function $g^{(2)}(t')$ can be written as [28]:

$$g^{(2)}(t') = B + \beta \exp\left(-2\bar{\Gamma}t' + K_2 t'^2 - \frac{K_3}{3}t'^3 + \dots\right)^2 \tag{58}$$

This function can be further optimized to [28]:

$$g^{(2)}(t') = B + \beta \exp\left(-2\bar{\Gamma}t'\right)\left(1 + \frac{K_2}{2!}t'^2 - \frac{K_3}{3!}t'^3 + \dots\right)^2 \tag{59}$$

Which also allows for direct fitting to $g^{(2)}$ data and eliminates some stability issues, which may arise using equation (58) [28]. Using the first cumulant $\bar{\Gamma}$, which corresponds to the mean of the decay rate distribution and is inversely related to the correlation time, one can determine a mean effective particle radius [29]:

$$R_{\text{eff}} = \frac{k_B T}{6\pi\eta} \cdot \frac{\boldsymbol{q}^2}{\bar{\Gamma}} \tag{60}$$

Since the cumulant model assumes a distribution centered around the mean decay rate, it can be used to derive limited information about the underlying size distribution. One useful indicator is the second cumulant K_2, which can be used as a measure for polydispersity. It is used to define the polydispersity index γ, which is calculated as:

$$\gamma = \frac{K_2}{\bar{\Gamma}^2} \tag{61}$$

This value corresponds to the normalized variance of the decay rate distribution $G(\Gamma)$. While thresholds vary, values of $\gamma < 0.05$ typically suggest a fairly narrow and therefore monodisperse distribution. It is important to note that the cumulant model describes the *distribution of decay rates*, not particle sizes. Since the relationship between decay rate and radius is nonlinear $\Gamma \propto 1/R$, obtaining the actual size distribution is not straightforward and generally requires model-based fitting or numerical inversion techniques. [30]

In essence, this means that there are multiple ways to make assumptions about the particle size distribution in DLS analysis. However, the primary objective, determining a realistic hydrodynamic radius, remains challenging. This is because, when fitting models such as a single exponential, a KWW function, or a cumulant model to the correlation data, one typically extracts only an average hydrodynamic radius. While this approach is straightforward, it introduces a significant bias toward larger particles, especially in the

Rayleigh scattering regime. As discussed, the scattering intensity in this regime increases with the sixth power of the particle radius. This means that even a small number of larger particles can dominate the measured signal, disproportionately influencing the decay time and the derived average radius. As a result, one must be cautious when interpreting what is actually being measured. A more modern approach to addressing this issue is offered by the CONTIN algorithm. Like the cumulant method, CONTIN models the field autocorrelation function as a distribution of decay rates, but unlike the cumulant approach, it does not assume this distribution to be Gaussian. Instead, CONTIN numerically solves the inverse Laplace transform using regularization techniques to stabilize the solution. This results in an estimate of the decay rate distribution, $G(\Gamma)$, which can then be converted to a hydrodynamic radius distribution by applying the Stokes–Einstein relation to each individual Γ value. [24], [31]

4.2. Analyzing Emulsion Stability

With the particle radius now determined from the autocorrelation data at various time points, this information can be used to assess the stability of the emulsion. If the particle radius remains constant over time, the emulsion may be considered stable. In contrast, an increase in particle radius suggests instability, at least up to a certain critical size. The dominant growth mechanism within the emulsion can be assessed by comparing experimental data with theoretical models. Namely, Ostwald ripening and coalescence. For Ostwald ripening, the relationship between droplet radius r and time t is given by equation (2). Taking the natural logarithm of both sides yields:

$$\ln(r) = \frac{1}{3}\ln(t) + \frac{1}{3}\ln\left(\frac{8}{9}\,\frac{c(\infty)\gamma V_m D}{\rho RT}\right) \tag{62}$$

The second logarithmic term is constant and can be summarized as $\ln(A)$, giving:

$$\ln(r) = \frac{1}{3}\ln(t) + \frac{1}{3}\ln(A) \tag{63}$$

In contrast, coalescence typically follows a linear time dependence, $r \propto t$. Taking the

logarithm gives:

$$\ln(r) = \ln(t) + \ln(A) \tag{64}$$

Therefore, by fitting a linear model to a plot of $\ln(r)$ versus $\ln(t)$, the slope of the fit can be used to distinguish between the two mechanisms.

4.3. Measurement Uncertainties and Errors

The standard deviation of the particle radius is determined based on the uncertainty in the correlation time τ. When fitting the autocorrelation data using either a single exponential model or a KWW function, the standard deviation of τ is obtained from the corresponding diagonal element of the covariance matrix returned by the fitting algorithm. Subsequently, Gaussian error propagation is applied to compute the standard deviation of the particle radius. Uncertainties in other parameters such as viscosity, temperature, and laser wavelength are neglected, as their contributions are assumed to be negligible compared to the uncertainty in τ. Using the cumulant model the standard deviation of τ can be calculated via the cumulants: $\sigma_\tau = \frac{\sqrt{K_2}}{\bar{\Gamma}^2}$ [30]. For specific time dependent measurements, particle radii are averaged over multiple measurements, where the uncertainty is calculated using Gaußian error propagation over the statistical uncertainty and the uncertainty from the fit.

As mentioned in the Methods section, errors may arise during sample preparation. If the sample becomes contaminated with dust, typically several orders of magnitude larger than the nanoparticles in the emulsion, it can scatter a substantial amount of light. This excessive scattering may overshadow the intensity of light scattered by the nanoparticles, leading to correlation times significantly larger than what is expected from the nanoparticles themselves. However, this issue can be easily addressed during data evaluation. Since hundreds of measurements are typically performed, any increase in correlation time caused by dust contamination appears as a clear outlier when plotting the correlation times across all measurements. A filtering mechanism is added to the code for data analysis that automatically excludes data points exceeding a defined threshold.

4.4. Goodness of Fit

Once the result from the fit are obtained, the goodness of fit can be analyzed briefly, by determining the distribution of residuals, which are give as:

$$\varepsilon_i = g^{(2)}(t'_i) - f(t'_i) \tag{65}$$

Where $g^{(2)}(t')$ corresponds to the function describing the measured datapoints, while $f(t')$ are the values of the correlation function, calculated using the parameters of the fit. Generally, one can determine the goodness of fit by the kind of distribution of these residuals. A random distribution of residuals supports a good fit, while a non-random distribution may indicate software problems. [24]

5. Testing Setup and Models on Reference Materials

Before conducting measurements on the thymol samples, the experimental setup and various models are validated using a reference material. The reference consists of polymer microspheres suspended in water, with a particle radius of $r = 125.0 \pm 6.8$ nm. The sample is diluted with additional distilled water and measured using the experimental setup described in Section 3.1. Measurements are performed at a temperature of 293 K, corresponding to a viscosity of 1.0016 mPa s. The autocorrelation function is calculated using the algorithm presented in Equation (42).

In this section, the different models used for fitting the reference material are compared. Specifically, the classic exponential model for monodisperse particle distributions in Equation (49), the KWW function in Equation (50), and the cumulant model in Equation (59) are considered.

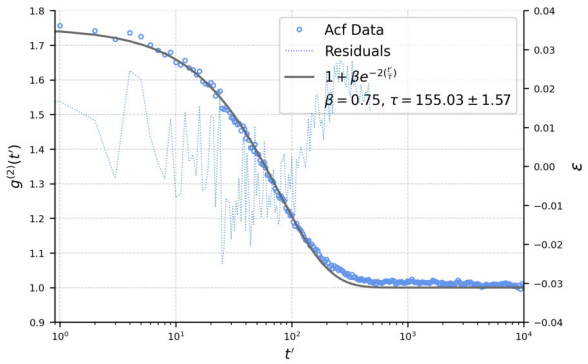

(a) Acf data fitted using a single exponential.

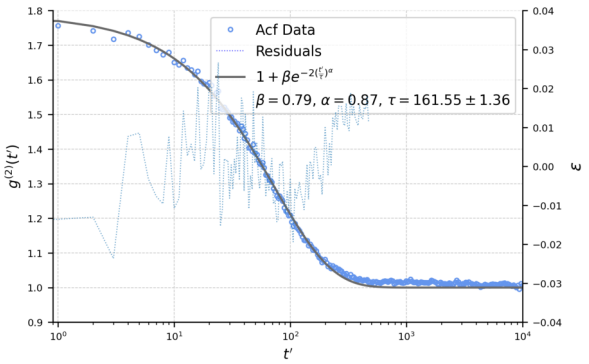

(b) Fit using a KWW function.

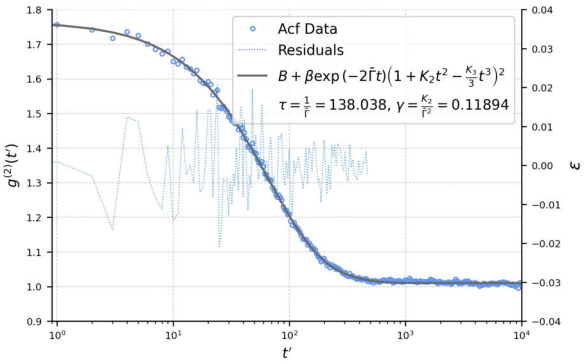

(c) Fit using a cumulant model.

Figure 6: Comparison of different models on ACF values of a standard. The time t' corresponds to a channel with a 30 µs width.

As observed, the classical exponential fit in Figure 6a does not perfectly align with the autocorrelation data. Calculating the particle radius from the extracted correlation time yields a value of $r = 140.2 \pm 1.1$ nm, which lies outside the standard deviation of the reference value. Figure 6b illustrates the fit using the KWW function.

The KWW fit in Figure 6b shows a noticeably improved alignment with the autocorrelation data. However, the resulting particle radius differs only marginally from that obtained using the exponential model, resulting in $r = 142.49 \pm 0.82$ nm.

Figure 6c presents the fit using the cumulant function. Calculating the particle radius from the cumulant fit yields $r = 122.8 \pm 1.4$ nm. This value lies within the standard deviation of the reference particle radius. Additionally, the resulting distribution of mean decay rates is extremely narrow, which is to be expected as the standard should be close to monodisperse. Figure 7 again shows all different fit models plotted onto the same datapoints for better visual comparison.

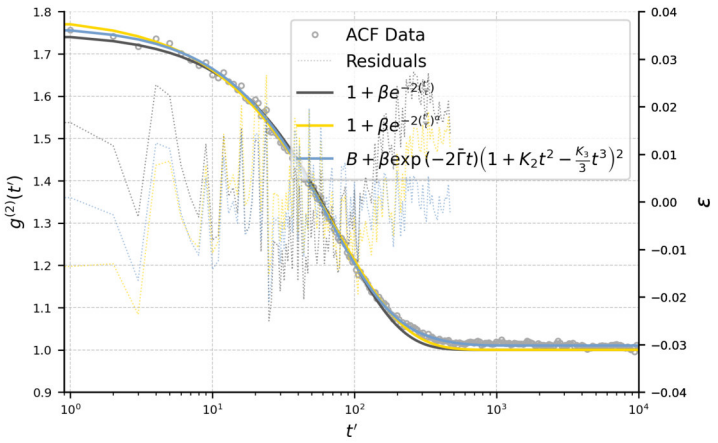

Figure 7: Comparison of single exponential, KWW function and cumulant function.

The overestimation of particle radii obtained using the single-exponential and KWW function is likely due to the use of an aged standard. The standard may have undergone degradation over time, leading to a significantly larger deviation from its size distribution than originally specified.

6. Results

The measurements were conducted in the following order. First, we examined the potential for spontaneous emulsification in thymol–ethanol–water systems and identified the concentration ranges where this phenomenon occurs. A 1:10 thymol-to-ethanol mixture was prepared and subsequently diluted with water to various concentrations.

If no spontaneous emulsification was observed at a given concentration, a high-energy emulsification method was employed. The mixture was sonicated in three intervals, totaling 24 minutes, to induce emulsification. This procedure was repeated across different concentrations while maintaining the fixed thymol-to-ethanol ratio.

DLS was used to monitor changes in particle size over time. These measurements served two purposes. First, to assess the stability of the dispersed particles and secondly, to determine whether the particle sizes fell within the micrometer range, enabling further investigation via optical microscopy to determine whether the system forms dispersed oil droplets due to localized solubilization of thymol by ethanol, or if thymol instead precipitates out of the mixture.

Subsequently, temperature-dependent DLS measurements were conducted to assess the influence of thermal conditions on particle size and stability.

Given that previous studies report the minimum inhibitory concentration (MIC) of thymol to be between 0.02–0.05% for bacteria and 0.004–0.05% for fungi [4], samples were diluted to concentrations both within and above this MIC range for further analysis.

6.1. Short time scale spontaneous emulsification at different composition of thymol-ethanol-water systems.

The prepared samples are measured directly after preparation using DLS with measurement times of two minutes and 30 seconds. Each channel t' corresponds to a time interval of 30 µs. At least 15 measurements are performed for each sample. The composition of each prepared sample is shown in Figure 8. The final autocorrelation function for each measurement is depicted in Figure 9.

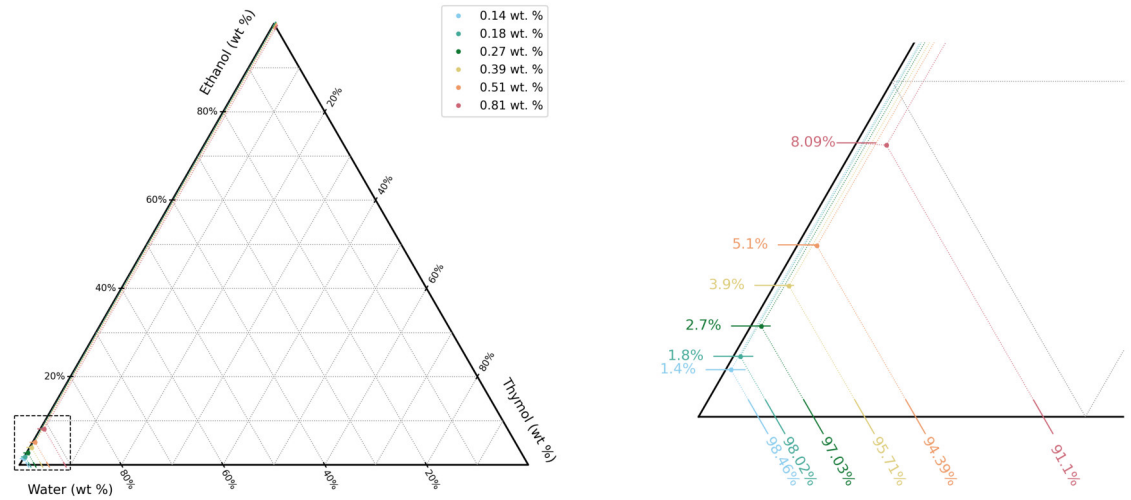

(a) Ternary plot of compositions. Labeled with weight percentage of thymol in the solution.

(b) Zoom to dashed region in the ternary phase diagram.

Figure 8: Ternary plots of different compositions.

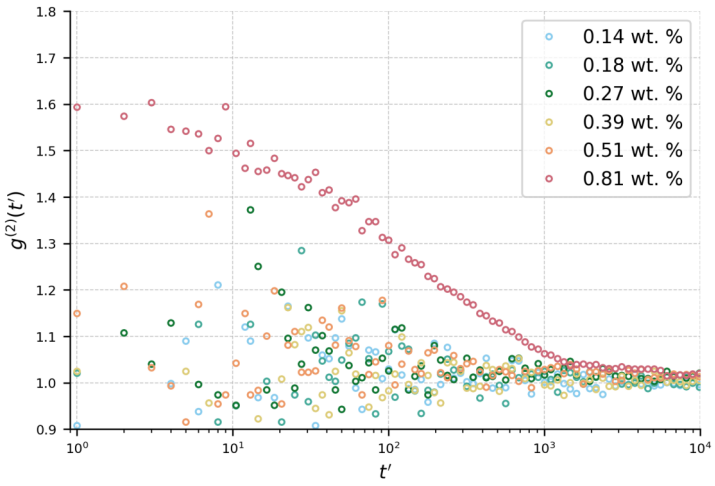

Figure 9: Autocorrelation function for different compositions.

Upon dilution of the thymol–ethanol mixture with water in the absence of high energy input, visible droplet formation occurred at all tested concentrations, with sub-millimeter droplets apparent to the naked eye. However, DLS only yielded a well-defined correlation function at the highest concentration, suggesting a change in either the droplet size distribution or the concentration of scatterers. At this concentration, the measured hydrodynamic radius was $r = 2.15$ µm, based on a fit using a KWW model, which also gave an exponential factor of $\alpha = 0.45$, indicative of a broad relaxation time distribution. In addition, the cumulant analysis returned a polydispersity index of $\gamma > 1$, consistent with an extremely polydisperse system. The DLS data, together with the visual observation of large droplets and absence of macroscopic precipitation, support the interpretation that spontaneous emulsification occurs upon dilution, likely driven by localized solubilization of thymol by ethanol. The emergence of measurable micrometer-sized particles at the highest concentration may reflect a shift toward larger or more stable droplets in this regime, though further analysis would be needed to fully resolve the underlying size distribution.

6.2. Short time scale high energy emulsification at different composition of thymol-ethanol-water systems.

Samples with similar concentrations are prepared again, this time with an additional sonication steps. For each sample sonication lasting 8 minutes is performed. This is repeated 3 times. The relative amount of each substance in the prepared samples can be seen in the ternary phase diagram in figure 10. Again, the samples are measured after preparation. The measurement time, channels and intervalls are identical to the previous measurement. Figure 11 shows the final autocorrelation function for each measurement.

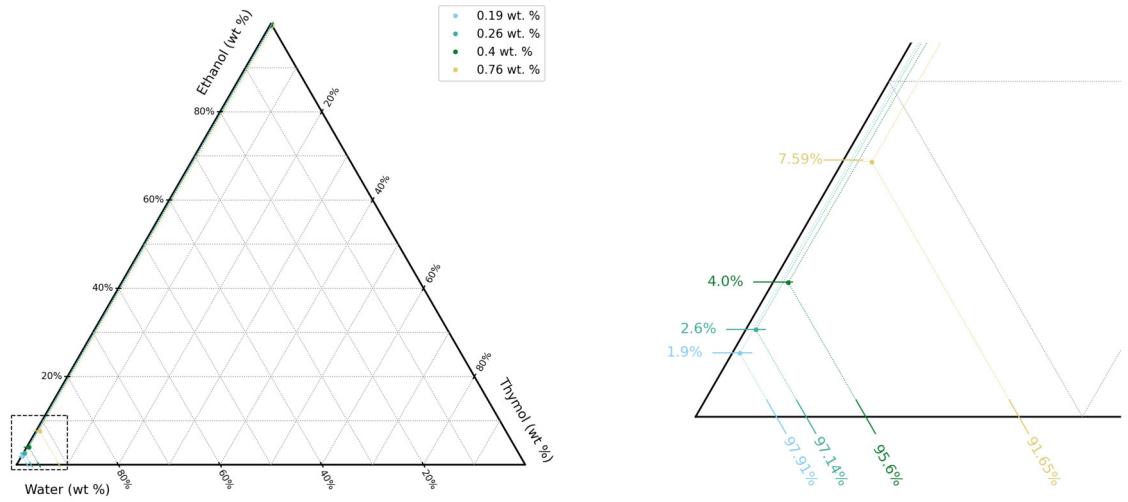

(a) Ternary plot of compositions. Labeled with weight percentage of thymol in the solution.

(b) Zoom to dashed region in the ternary phase diagram.

Figure 10: Ternary plots of different compositions.

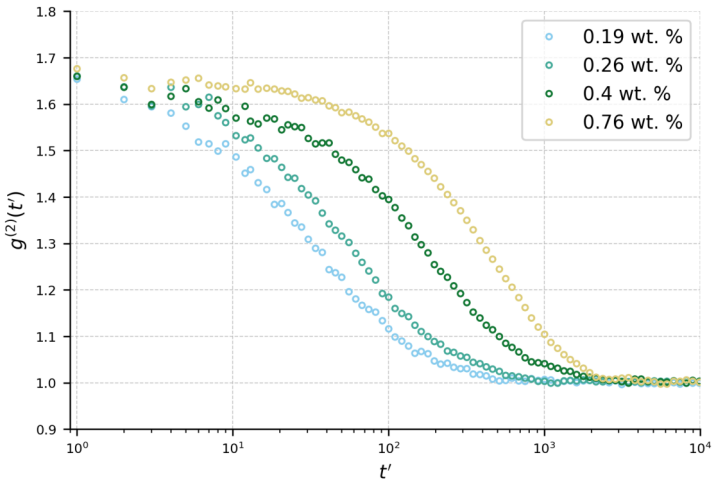

Figure 11: Autocorrelation function for different compositions.

Following the application of external energy input via sonication, the samples exhibited a mist-like, milky appearance visible to the naked eye, suggesting the formation of smaller dispersed particles. As shown in Figure 11, all measured concentrations produced a decaying autocorrelation function, indicating the presence of particles within the detectable size range of DLS. This supports the interpretation that sonication leads to significantly smaller particle formation compared to spontaneous droplet dispersion. The autocorrelation functions were again fitted using a KWW model, and the resulting hydrodynamic

radii and corresponding α values are presented in figure 12.

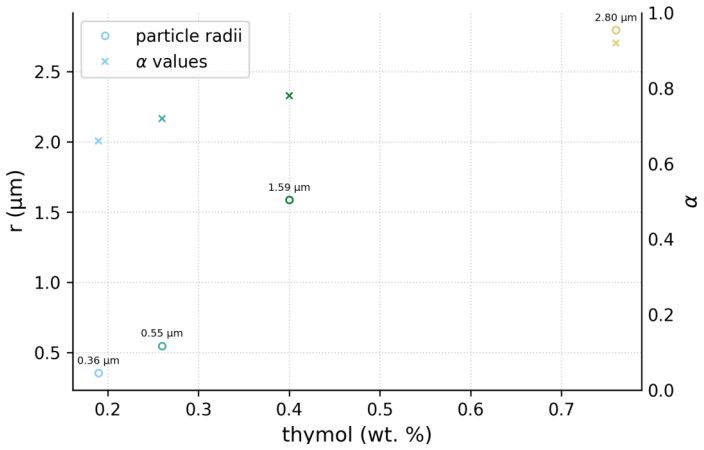

Figure 12: Particle radii r and corresponding α values for the autocorrelation functions in figure 11.

The results clearly demonstrate a dependence of particle size on thymol concentration, with larger particles observed at higher concentrations. The associated α values suggest that lower concentrations may exhibit broader particle size distributions; however, whether this reflects a true physical difference or arises from limitations in DLS resolution at larger particle sizes will be discussed in the following chapter.

6.3. Medium time scale high energy emulsion at different composition of thymol-ethanol-water systems.

Having confirmed that particles in the nano- to micrometer range can be formed across different concentrations using external energy input, the same method was employed to investigate the properties of these particles further. Similar concentrations to those previously used were obtained by diluting a thymol–ethanol mixture with distilled water. The samples were analyzed using DLS, maintaining the same number of channels and measurement intervals as in previous experiments. This time, however, measurements were carried out continuously over longer periods, lasting up to three days, to observe time dependent changes in particle size.

Figure 13 depicts the measured compositions for the medium time scale measurements. While figure 14 shows the evolution of hydrodynamic radius over time for each concentra-

tion. The hydrodynamic radii are again determined using a KWW model.

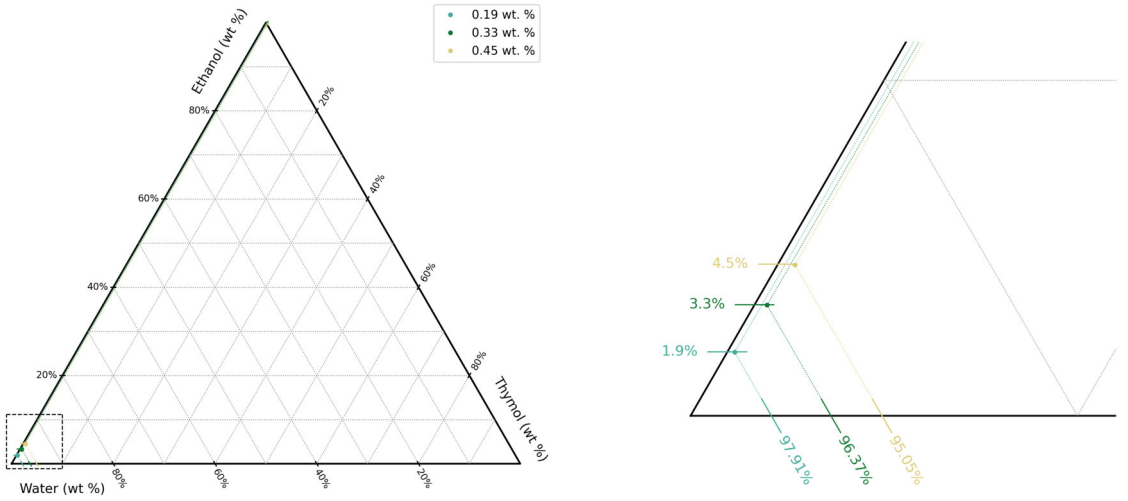

(a) Ternary plot of compositions. Labeled with weight percentage of thymol in the solution.

(b) Zoom to dashed region in the ternary phase diagram.

Figure 13: Ternary plots of different compositions.

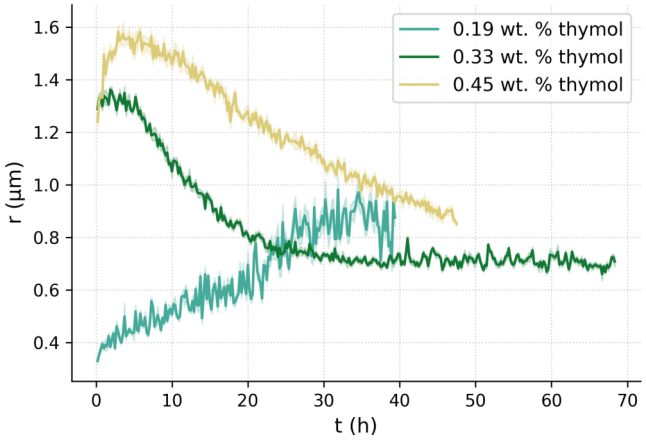

Figure 14: Hydrodynamic radius of thymol particles in time. The radii are averaged over 5 measurements. The shaded area corresponds to one standard deviation.

Interpreting the data from the time dependent plot is not straightforward at all. Depending on the composition, it seems that there is either an increase or a decrease in the hydrodynamic radius, which is very unusual. It is more probable that DLS will stop being a suitable method for measurement at the particle size resulting from the composition used,

as the particles will become too large for their movement to be dominated by Brownian motion. As larger particles coalesce, or ripen they do not contribute to the measurement of relaxation times anymore. Smaller particles, then become dominant in the signal. A similar conclusion can be drawn from the measurement of total intensities in figure 15.

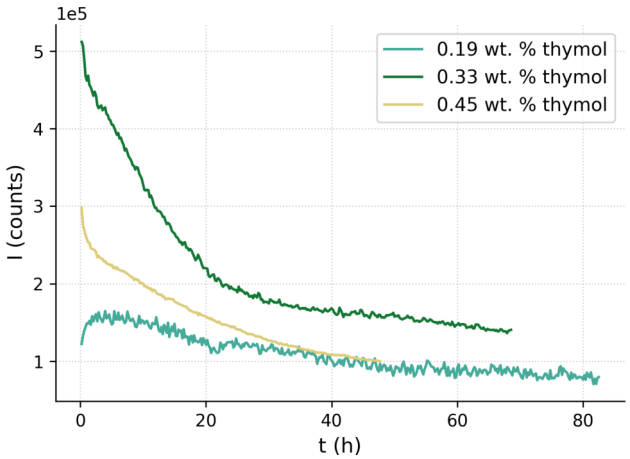

Figure 15: Total intensities averaged over 5 measurements for different compositions of thymol, ethanol and water over time.

While the total intensity remains roughly constant for the solution with the lowest weight percent and steadily increasing particle size, the other two measurements exhibit a significant decrease in total intensity over time. This observation supports the assumption that, as particles grow larger, gravitational forces begin to dominate over Brownian motion. As a result, the particles settle out of the incident laser beam, leading to a decrease in the measured total intensity. A similar conclusion can also be drawn from the α value using a KWW fit in figure 16.

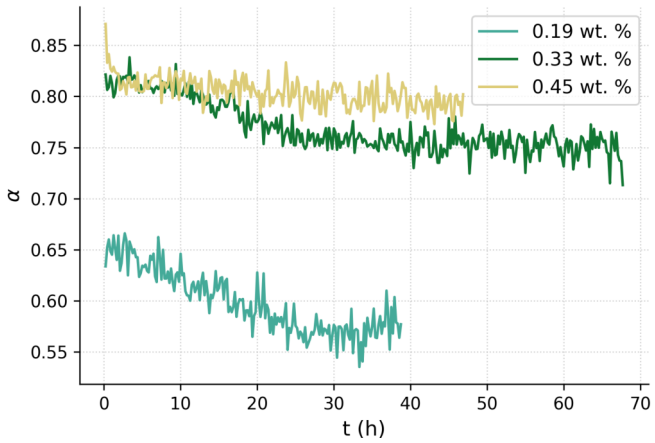

Figure 16: Change in polydispersity over time, modeled using the exponential factor α from a KWW fit.

The change in the α factor suggests that the polydispersity of the higher-concentration composition remains low and relatively constant over time, whereas polydispersity increases in the solution with the lowest thymol concentration. However, it is possible that, in the case of the higher-concentration composition, we are only observing the lower tail of the particle size distribution.

As the particles approach the micrometer scale, they become observable through microscopic imaging. Which in some way is also fortunate as this allows for the assessment of the dispersion behavior of thymol–ethanol–water systems, as discussed in Section 2.2. Figure 17 shows a microscopic image of the sample. Measurements were taken with a Zeiss Axio Imager 2, at the Faculty Center for Nano Structure Research at the University of Vienna.

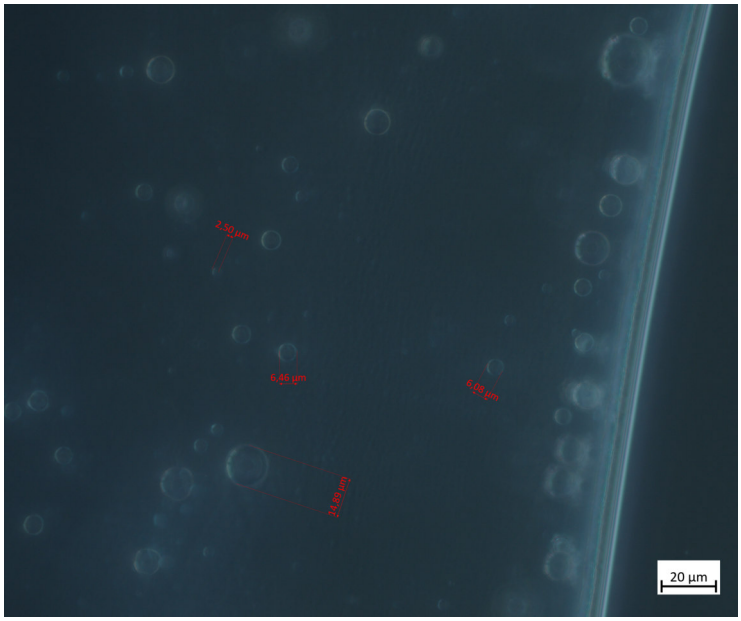

Figure 17: Emulsion under optical microscope using using dark field epi-illumination.

The microscopic imaging clearly shows the formation of droplets rather than precipates, supporting that the idea of locally solvated thymol may be correct. Which in itself is already a great result regarding pharmaceutical use. On the other hand, the particles are indeed in the micrometer range, which limits the use of DLS for reliable measurements. As a result, only the composition with the lowest thymol weight percentage can be used for further analysis, as it remains within the measurable range of DLS and allows tracking of particle growth to assess emulsion stability.

6.4. Medium time scale temperature dependent measurements at identical composition of thymol-ethanol-water systems

With a suitable composition for time-dependent particle formation now established, it is used to investigate the underlying growth mechanisms within the emulsion and to assess their dependence on temperature. The goal is to identify whether a specific temperature range exists in which a stable emulsion can be maintained. To this end, multiple compositions containing 0.19 wt % thymol were prepared and measured using DLS at various temperatures over periods of up to one week. Measurements were discontinued once the particle radius reached approximately 1µm. The evolution of hydrodynamic radii over time at different temperatures is shown in figure 18.

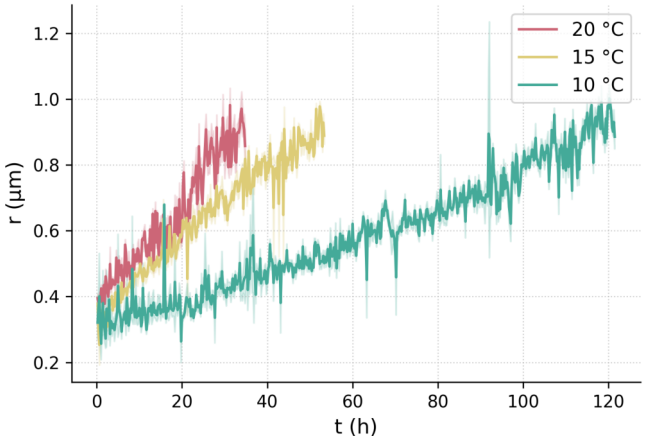

Figure 18: The changes in the hydrodynamic radius are plotted for different temperatures. Measurement is stopped when critical particle size is reached.

As evident from the plots, none of the tested temperatures resulted in a fully stable emulsion; all samples exhibited particle growth over time, with a strong temperature dependence. However, at 10 °C, particle sizes remained within the nanometer range for at least 24 hours, indicating significantly slower growth at lower temperatures. To further investigate the underlying growth mechanism, both the hydrodynamic radii and time were logarithmically transformed, and a linear fit was applied to the resulting data, as shown in figure 19.

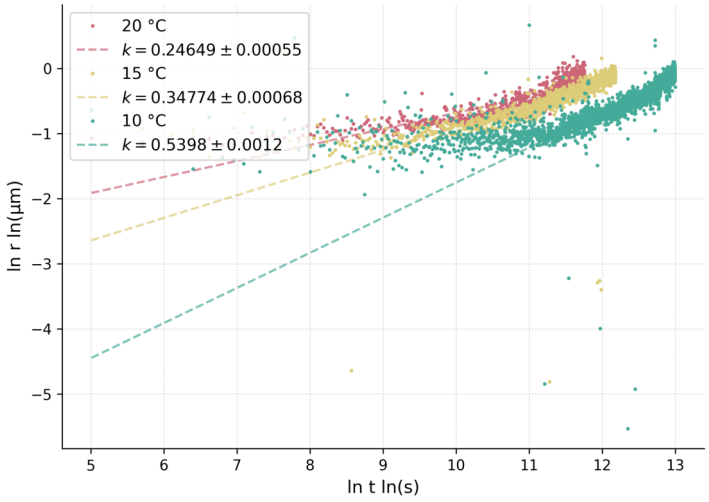

Figure 19: Linear fit on double logarithmically plotted changes in particle radii for different temperatures.

Interestingly, the highest growth exponent of approximately 0.54 was observed at the lowest temperature 10 °C, which appears counterintuitive given that both Ostwald ripening and coalescence typically accelerate with temperature. This result may be influenced by several factors. First, the measurements at lower temperatures could be less accurate due to slower dynamics and smaller initial particle sizes, which may affect the quality of the fit in the early stages. It is also possible that the growth at low temperature starts more slowly and then speeds up, leading to a steeper slope over the measured time range. Another explanation could be that different growth mechanisms are active at different temperatures, or that the system at low temperature follows a different coarsening behavior altogether.

7. Conclusions and Outlook

While the exact mechanism remains unclear, the observed dispersion behavior of thymol, ethanol, and water forming liquid-like droplets ranging from nanometer to micrometer sizes depending on composition is on itself a promising result. Droplets within this size range are known to potentially exhibit enhanced bioactivity, which could translate into improved antibacterial properties of the active compound. However, this hypothesis requires verification through antimicrobial screening.

It is unfortunate that particle distributions in the nanometer range could not be achieved via spontaneous emulsification upon dilution with water. Spontaneously formed dispersions might offer more stable particles compared to those created through external energy input. Whether such spontaneous formation is feasible cannot be determined within the scope of this thesis, as the ethanol to thymol ratio was kept constant. A complete ternary phase diagram exploring variable proportions of all components would exceed the limits of a master's thesis, but future research could investigate whether different compositions lead to the formation of nanometer sized droplets.

The nanometer-sized droplets formed in this study remained stable for at least 24 hours, which may already be sufficient for preliminary antimicrobial screening. Importantly, this stability was achieved without the use of surfactants, making it worthwhile to further explore the influence of such systems on antibacterial and antifungal efficacy.

Overall, these findings provide a valuable foundation for developing surfactant-free, bioactive emulsions of thymol, and future research may find new opportunities for antimicrobial formulations based on thymol dispersions.

8. References

[1] Anna Marchese et al. “Antibacterial and antifungal activities of thymol: A brief review of the literature”. In: *Food chemistry* 210 (2016), pp. 402–414.

[2] Elise Lepeltier, Claudie Bourgaux, and Patrick Couvreur. “Nanoprecipitation and the “Ouzo effect”: Application to drug delivery devices”. In: *Advanced Drug Delivery Reviews* 71 (2014), pp. 86–97.

[3] Shoichi Gohtani and Waraporn Prasert. “Nano-Emulsions; Emulsification Using Low Energy Methods”. In: *Japan Journal of Food Engineering* 15.3 (2014), pp. 119–130.

[4] Jianming Li et al. “Thymol nanoemulsions formed via spontaneous emulsification: Physical and antimicrobial properties”. In: *Food chemistry* 232 (2017), pp. 191–197.

[5] Maria A Vratsanos et al. “Ouzo effect examined at the nanoscale via direct observation of droplet nucleation and morphology”. In: *ACS Central Science* 9.3 (2023), pp. 457–465.

[6] Conxita Solans, Daniel Morales, and Maria Homs. “Spontaneous emulsification”. In: *Current Opinion in Colloid & Interface Science* 22 (2016), pp. 88–93.

[7] Elijah Nazarzadeh, Tania Anthonypillai, and Shahriar Sajjadi. “On the growth mechanisms of nanoemulsions”. In: *Journal of colloid and interface science* 397 (2013), pp. 154–162.

[8] Tharwat Tadros et al. “Formation and stability of nano-emulsions”. In: *Advances in colloid and interface science* 108 (2004), pp. 303–318.

[9] Lorenz-M. Stadler et al. “Long-term correlations distinguish coarsening mechanisms in alloys”. In: *Phys. Rev. B* 68 18 (2003), p. 180101.

[10] Peipei Zhu et al. “Solubility and solution thermodynamics of thymol in six pure organic solvents”. In: *The Journal of Chemical Thermodynamics* 92 (2016), pp. 198–206.

[11] Jean-Pierre Hansen and Ian R. McDonald. *Theory of Simple Liquids*. 3rd. Amsterdam: Academic Press, (2006).

[12] P. N. Pusey. “Introduction to Scattering Experiments”. In: *Neutrons, X-rays and Light: Scattering Methods Applied to Soft Condensed Matter*. Ed. by P. Lindner and Th. Zemb. Amsterdam: North-Holland, (2002), pp. 1–22.

[13] Stefan U. Egelhaaf and Peter N. Pusey. “Dynamic Light Scattering”. In: *Neutrons, X-rays and Light: Scattering Methods Applied to Soft Condensed Matter*. Ed. by Peter Lindner and Julian Oberdisse. Amsterdam: Elsevier, (2024), pp. 211–238.

[14] Bruce J. Berne and Robert Pecora. *Dynamic Light Scattering: With Applications to Chemistry, Biology, and Physics*. Unabridged. Mineola, NY: Dover Publications, (2000).

[15] Peter Atkins and Julio de Paula. *Physical Chemistry*. 9th ed. New York: W. H. Freeman, (2010).

[16] Helmut Mehrer. "Diffusion: Introduction and Case Studies in Metals and Binary Alloys". In: *Diffusion in Condensed Matter: Methods, Materials, Models*. Ed. by Paul Heitjans and Jörg Kärger. Berlin, Heidelberg: Springer, (2005), pp. 3–63.

[17] Oleksandr Mykhaylyk. "General Theorems, Differential Scattering Cross-Section, and Initial Data Treatment". In: *Neutrons, X-rays and Light: Scattering Methods Applied to Soft Condensed Matter*. Ed. by P. N. Pusey. Elsevier, (2002). Chap. 2, pp. 49–134.

[18] Jörg Stetefeld, Sean A McKenna, and Trushar R Patel. "Dynamic light scattering: a practical guide and applications in biomedical sciences". In: *Biophysical reviews* 8 (2016), pp. 409–427.

[19] Alan V Oppenheim and George C Verghese. *Signals, systems & inference*. Pearson London, (2017).

[20] Alan V Oppenheim. *Discrete-time signal processing*. Pearson Education India, (1999).

[21] Sourav Bhattacharjee. "DLS and zeta potential–what they are and what they are not?" In: *Journal of controlled release* 235 (2016), pp. 337–351.

[22] Abolghasem Jouyban et al. "Calculation of the viscosity of binary liquids at various temperatures using Jouyban–Acree model". In: *Chemical and Pharmaceutical Bulletin* 53.5 (2005), pp. 519–523.

[23] Ibrahim Sadek Khattab et al. "Density, viscosity, and surface tension of water+ ethanol mixtures from 293 to 323K". In: *Korean Journal of Chemical Engineering* 29 (2012), pp. 812–817.

[24] Petr Štěpánek. "Data Analysis in Dynamic Light Scattering". In: *Dynamic Light Scattering: The Method and Some Applications*. Ed. by Wyn Brown. Oxford: Clarendon Press, (1993), pp. 177–241.

[25] Karl Fischer and Manfred Schmidt. "Pitfalls and novel applications of particle sizing by dynamic light scattering". In: *Biomaterials* 98 (2016), pp. 79–91.

[26] JH Wu and Q Jia. "The heterogeneous energy landscape expression of KWW relaxation". In: *Scientific reports* 6.1 (2016), p. 20506.

[27] François Liénard, Éric Freyssingeas, and Pierre Borgnat. "A multiscale time-Laplace method to extract relaxation times from non-stationary dynamic light scattering signals". eng. In: *The Journal of chemical physics* 156.22 (2022), pp. 224901–224901.

[28] Barbara J Frisken. "Revisiting the method of cumulants for the analysis of dynamic light-scattering data". In: *Applied optics* 40.24 (2001), pp. 4087–4091.

[29] Dennis E Koppel. "Analysis of macromolecular polydispersity in intensity correlation spectroscopy: the method of cumulants". In: *The Journal of Chemical Physics* 57.11 (1972), pp. 4814–4820.

[30] Alastair G. Mailer, Paul S. Clegg, and Peter N. Pusey. "Particle sizing by dynamic light scattering: non-linear cumulant analysis". In: *School of Physics and Astronomy, University of Edinburgh* (2015).

[31] Matthew Salazar et al. "A user-friendly graphical user interface for dynamic light scattering data analysis". In: *Soft Matter* 19.34 (2023), pp. 6535–6544.

A. Python Code

The following Python functions were used to calculate the intensity autocorrelation as described in section 3.2

A.1. Direct Autocorrelation

```
import numpy as np

def autocorrelation(sequence):

    N = len(sequence)
    normalization = np.mean(sequence)**2  # <I(t)>^2
    g2_values = []

    for t in range(N - 1):
        # <I(t) * I(t + tau)>
        correlation = np.mean(sequence[:N - t] * sequence[t:])
        g2 = correlation / normalization
        g2_values.append(g2)

    return np.array(g2_values)
```

A.2. FFT-Based Autocorrelation with Binning

```
def autocorrelation_fft(sequence, binning=None):

    N = len(sequence)
    normalization = np.mean(sequence)**2  # <I(t)>^2

    # Zero-padding to avoid convolution artifacts
    pad = 2 * N
    sequence_fft = np.fft.fft(sequence, pad)
    psd = sequence_fft * np.conjugate(sequence_fft)
    correlation_padded = 1 / N * np.real(np.fft.ifft(psd))
    correlation = correlation_padded[:N]
```

```
    g2_values = correlation / normalization

    if binning is None:
        return g2_values, np.arange(len(g2_values))

    # Logarithmic binning
    start = 1
    ratio = binning
    bins = [start]
    while bins[-1] < N:
        bins.append(bins[-1] * ratio)
    bins = np.unique(np.array(bins).astype(int))

    binned_g2 = np.zeros(len(bins) - 1)
    bin_centers = np.zeros(len(bins) - 1)

    for i in range(len(bins) - 1):
        start, end = bins[i], bins[i + 1]
        binned_g2[i] = np.mean(g2_values[start:end])
        bin_centers[i] = (end + start) / 2.0

    return binned_g2, bin_centers - 3 / 2  # start ~ 0
```

The complete code used for data analysis and visualization, including viscosity calculations, data fitting, automated radius determination over extended time periods, and the creation of ternary plots etc., is available at github.com/Elias-Ploe/DLS.

B. Licenses Elsevier

This license agreement is made between **Elias Plöchl** ("You") and **Elsevier** ("Elsevier"). It consists of your license details and the terms and conditions provided by Elsevier and the Copyright Clearance Center.

License Number:	6056560054464
License Date:	June 26, 2025
Licensed Content Publisher:	Elsevier
Licensed Content Publication:	*Current Opinion in Colloid & Interface Science*
Licensed Content Title:	*Spontaneous emulsification*
Licensed Content Authors:	Conxita Solans, Daniel Morales, Maria Homs
Licensed Content Date:	April 1, 2016
Licensed Content Volume:	22
Licensed Content Issue:	n/a
Licensed Content Pages:	88–93
Type of Use:	Reuse in a thesis/dissertation
Portion:	Figures/Tables/Illustrations
Date of Agreement Confirmation:	July 17, 2025